International Journal of Civil Engineering

Structure-Concrete

Cyclic performance of concrete-encased composite columns with T-shaped steel sections

Ch. Xu[1], L. Zeng[1,*], Q. Zhou[1], X. Tu[1], Y. Wu[1]

Received: September 2013, Revised: January 2015, Accepted: July 2015

Abstract

To study seismic performance of concrete-encased composite columns with T-shaped steel cross-section, twelve half-scale columns were tested under quasi-stastic cyclic loading. The result indicates that concrete-encased composite columns with T-shaped steel section possess good seismic performance. The failure modes include bending failure, shear-bond failure, shear compression failure and shear-composition failure. Unsymmetrical phenomenon of positive and negative hysteresis loop was shown evidently. Span ratio has a great influence on failure mode. The ductility performance decreases with increasing of axial compression level. As stirrup ratio increases, ductility and bearing capacity of columns are improved greatly, and energy dissipation capacity after yielding is enhanced. Cross tie can enhance ultimate bearing capacity, and lower strength attenuation and stiffness degradation on the later loading stage.

Keywords: *Concrete-encased composite column, Unsymmetrical, Seismic behavior, Experimental study.*

1. Introduction

Concrete-encased composite structure, which has been widely used in super-high building structures and large-span structures, possess advantages of high load-carrying capacity, good seismic performance, etc.[1-4]. Fig. 1 shows that section form and structural steel shape of concrete-encased steel composite columns are varied. There are symmetrical and unsymmetrical steel cross sections according to different forced state. In practical engineering, a structural steel with symmetrical steel section is generally used in an inner column of the composite building, a structural steel with T-or L-shaped steel section is generally used in corner columns and border columns to satisfy uneven forced state.

Many studies have been conducted for concrete-encased composite columns with symmetrical steel section to investigate the axial load-carrying capacity[5], behaviour under uniaxial bending and axial compressive load[6,7], behaviour under biaxial bending and axial compressive load[8-11], behavior under cyclic horizontal load and axial compressive load[12-15], behavior under high temperature[16,17], Numerical simulation method[18,19]. The design calculation theory and construction method are given in building codes such as ACI 318-05code, JGJ 138-2001 specification, AIJ-SRC standard and AISC Manual of Steel Construction[20-24].

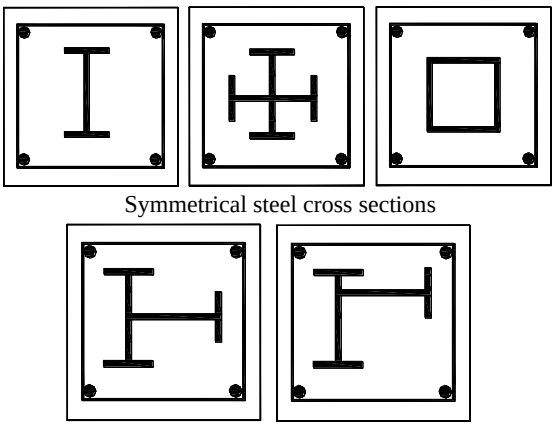

Symmetrical steel cross sections

Unsymmetrical steel cross sections

Fig. 1 Types of concrete-encased steel composite column

However, very few methods and experimental researches are available for concrete-encased composite columns with unsymmetrical steel section. Existing achievements mainly focused on calculation method of bending strength. Based on the ultimate strength curve, a simplified approach for bending strength of concrete-encased composite columns with unsymmetrical steel was proposed by modifying the calculation method of bidirectional symmetrical steel given in the EUROCODE 4[25,26]. However, the analysis only involves unidirectional symmetrical steel section but doesn't give corresponding information about bidirectional unsymmetrical steel section such as T-shaped and L-shaped steel, etc.

There are seldom researches on seismic behavior and failure mechanism of concrete-encased composite column

** Corresponding author: zenglei@yangtzeu.edu.cn*
1 School of Urban Construction, Yangtze University, Jingzhou, 434023, P.R. China

with T-shaped steel section. The correlative relationships between ductility, bearing capacity and factors of cross section form, structural steel shape, shaped steel ratio, shear span ratio, axial compression level, stirrup ratio, presence of cross tie are not found in building codes including the two China' s current regulations (JGJ 138-2001 2001; YB 9082-2006 2006) on composite structures, which can not provide technical support for engineering application.

This study carried out cyclic loading tests on twelve half-scale columns with T-shaped section steel. The test parameters included shear span ratio, axial compression level, stirrup ratio and presence of cross tie. Mechanical process, failure mode, strain distribution, hysteretic characteristics, skeleton curves, ductility and energy dissipation capacity were taken into comparison. The author hopes to provide references for engineering application of concrete-encased composite column with unsymmetrical steel section.

2. Experimental Program

2.1. Test Specimens

Twelve columns with T-shaped steel section were designed to represent approximately a half-scale model of a prototype column used in medium-rise buildings. The test specimens had a square cross section of 300×300 mm. Fig. 2 shows the four configurations of cross sections. Table 1 shows the details of the twenty-four specimens included in the experimental program. The test specimens consisted of the structural steel, longitudinal reinforcement, transverse reinforcement and concrete. The variables studied included shear span ratio, spacing of the transverse ties, axial load level and cross ties.

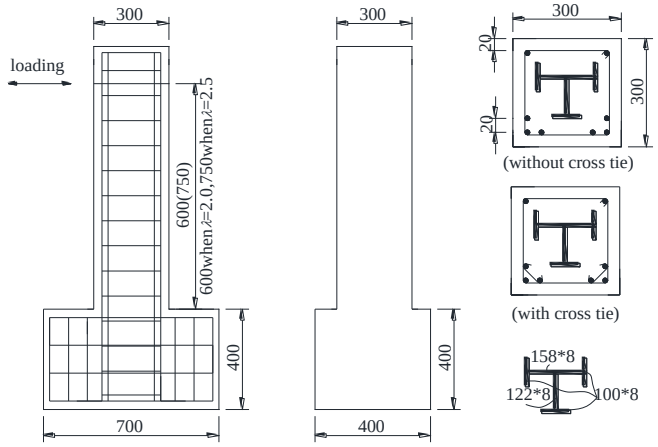

Fig. 2 Specimen dimension and steel details
Note: dimensions are in mm

Table 1 Parameters of specimens

Specimen	λ	Cross tie	Structural steel ratio(%)	Hoop spacing (mm)	Axial load level (% of *N*)
T-1	2.5	-	5.19	75	0.2
T-2	2.5	-	5.19	75	0.4
T-3	2.5	-	5.19	150	0.2
T-4	2.5	-	5.19	150	0.4
T-5	2.5	Yes	5.19	150	0.2
T-6	2.5	Yes	5.19	150	0.4
T-7	2.0	Yes	5.19	75	0.2
T-8	2.0	-	5.19	75	0.4
T-9	2.0	-	5.19	150	0.4
T-10	2.0	Yes	5.19	150	0.4
T-11	2.0	Yes	5.19	150	0.5
T-12	2.0	Yes	5.19	150	0.2

The T-shaped structural steel used in the specimens were consisted of several hot-rolled steel plates. The steel plates were welded to create a T-shaped steel section. The ratio of the structural steel area to the gross area was 5.19%. The shear span ratio, λ, shown in Table 1, which reflects the relative relationship between the subjected bending moment, M, and shear force, V, is defined as ratio of the height of specimens, L, to the total depth of the cross section, h.

$$\lambda = L / h = M /(V \cdot h) \tag{1}$$

As shown in Fig. 2, a longitudinal bar was placed at each corner of the columns. Four additional longitudinal bars, two at each lower corner, were added. These additional bars were intended to strength the weaker part of the section and provide a better confinement for the concrete core. In addition, cross ties of 14 mm in diameter were used at lower corners to engage the additional longitudinal bars and to enhance the deformation ductility of the column. The cross ties engaged the longitudinal bars through a seismic hook of 135° at one end and a 90° hook at the other end. Deformed bars of 8 mm in diameter were used as hoop reinforcement. Two different hoop spacing of 75 and 150 mm were used, which formed two levels of stirrup ratio.

The columns were subjected to constant axial load and

reversed cyclic lateral displacement. The magnitude of the applied axial load has four levels (n=0.20, 0.40, 0.50 and 0.60), which is defined as:

$$n = \frac{N}{f_c' A_c + F_y A_s + F_{yr} A_r} \quad (2)$$

Where N was axial load applied, A_c, A_s and A_r are area of concrete, steel and longitudinal bar respectively, f_y and f_{yr} are the specified yield strength of structural steel shape and longitudinal bar, and f_c' is concrete compressive strength.

2.2. Material property

The columns were constructed and tested at the civil engineering experiment center of Yangtze University. All specimens were tested at 28 days.

Premixed concrete was used. To determine the average concrete compressive strength three cylinders (150×300 mm) were tested for each specimen. The measured concrete compressive strength was 45.4MPa.

The longitudinal bar used was 14 mm in diameter and deformation. Deformation bars of 8 mm in diameter were used as hoop reinforcement and cross tie, which was to engage the longitudinal bars and to enhance the deformation ductility of the column. The results of the characterization tests following GB/T 228.1-2010 are shown in Table 2 [27]. To determinate the average values of the steel mechanical properties three pieces of reinforcing steel were tested for each nominal diameter.

Table 2 Materials properties of bars and steel plate

Material	Yield strength f_y (N/mm^2)	Ultimate strength f_u (N/mm^2)	Elastic modulus E_s (N/mm^2)
Φ8 bar	263	409	2.1×10^5
Φ14 bar	279	422	2.1×10^5
Steel plate	327	471	2.0×10^5

2.3. Test setup and test procedure

Fig. 3 shows the test-up for cyclic loading test. Upper end loading scheme was adopted, which can consider the P-Δ effect caused by the applied axial compressive load acting on the lateral displacement of the columns. The column specimens were subjected to a uniform compression load defined by formula 2 during cyclic lateral loading. The axial compressive load was applied by a hydraulic jack installed at the upper end of column and it remained constant. The lateral load was applied by a servo-controlled hydraulic actuator at the upper column end, using a displacement-controlled testing at a speed of 10 mm/min.

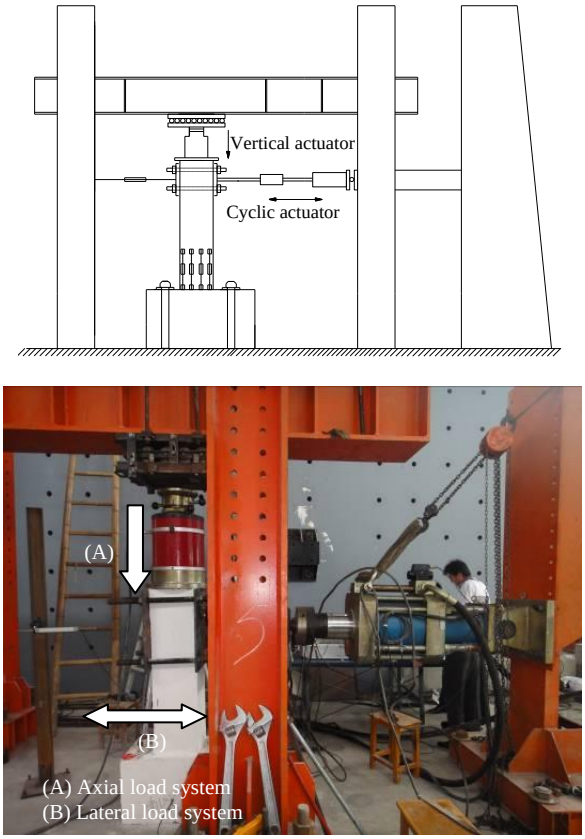

Fig. 3 Test set-up for cyclic loading test

The columns were laterally subjected to a predetermined cyclic displacement history as indicated in Fig. 4, which shows that the peak displacements were increased in multiples of the yielding displacement.

Load-lateral displacement hysteresis curve and the state of structural steel strain were observed to judge whether the specimen is yielded. The yielding displacement, Δ_y is the lateral displacement when the structural steel yield. A displacement ductility, u, is defined as ratio of applied lateral displacement, Δ, to the yielding displacement, Δ_y.

$$u = \Delta / \Delta_y \quad (3)$$

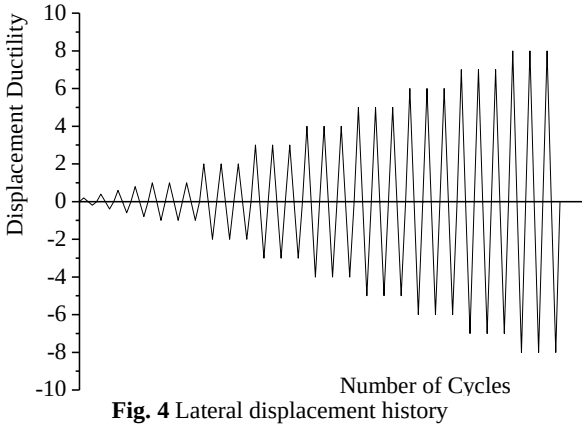

Fig. 4 Lateral displacement history

The specimens were subjected to one cycle before yielding and three successive cycles after yielding. The experiment stopped when the load falls to 85% ultimate load, or the specimens were unable to bear axial force.

2.4. Contents of measure

(1) Load-displacement at the end of column: Adopting a servo-controlled hydraulic jack with automatic constant pressure controlled, the top of the column was subjected to a lateral force. The lateral force on the top of the column was acquired by load-displacement sensor which connects with servo-controlled actuator, and the lateral displacement was measured by displacement meter.

(2) Strain distribution of concrete: As indicated in Fig. 5, attached strain gauges located at bottom end of columns were adopted to measure the strain of external concrete along the sectional depth, which aimed to understand the strain distribution at different loading stages and to verify whether the assumption of plane section for concrete-encased composite column with T-shaped steel section is established.

(3) Strain of structural steel and reinforcement: To investigate strain state in testing process, strain gauges and strain rosettes were arranged on the structural steel, longitudinal bars and hoops. Fig. 6 shows the direction of strain gauges attached on the steel and bars at the bottom end of columns.

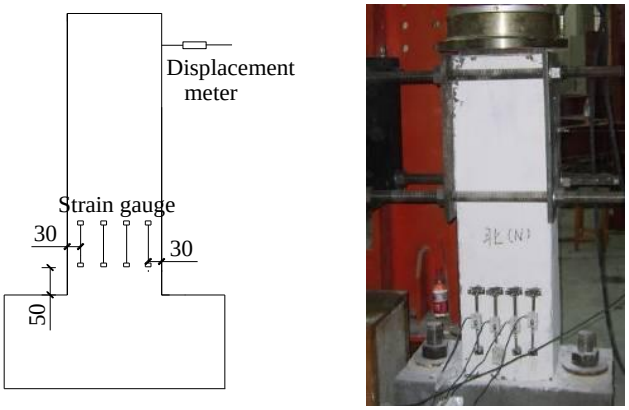

Fig. 5 Concrete strain measurement

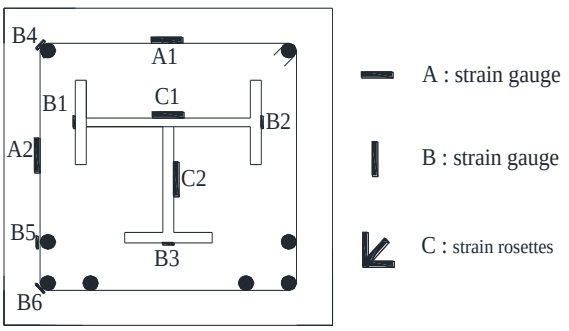

Fig. 6 Steel strain measurement

3 Experimental results and analysis

3.1. Experimental phenomena and failure mode

Failure modes of concrete-encased composite column with T-shaped steel section include bending failure, shear-bond failure, shear-compression failure and shear-composition failure under constant axial compressive load and cyclic lateral load. Fig. 7 shows the photographs of specimens at the end of the test.

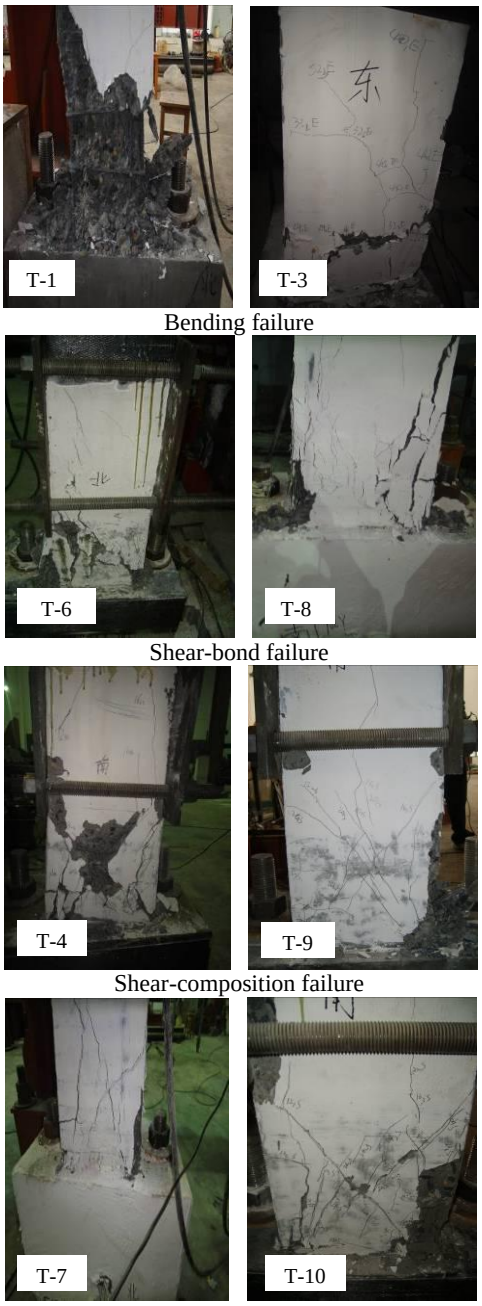

Fig. 7 Photographs showing the failure of specimens after test

Bending failure occurred in the specimens T1, T2, T3 and T5. Taking specimen T-1 as an example, its process was as follows. At the early loading stage, specimens were in elastic stage, the residual deformation was small when

unloaded. At cycles of $\mu = 0.5$, when the lateral load increased to about 40% of maximum load, horizontal concrete crack appeared on the tensile side at column bottom end, and longitudinal cracks appeared on the compressive side. As loading continues, horizontal concrete cracks extended to the front of columns. However, the cracks were resisted by steel flange and inclined upward slowly. At cycles of $\mu = 2$, a few incline concrete cracks appeared at the front of specimens, which were not apparent as horizontal cracks. Continue spread and close of horizontal cracks were caused by the cyclic loading and the crack width progressively grew. At cycles of $\mu = 3$, when the lateral load reaches approximately 80% of the maximum load, large-area external concrete on tensile side spalled following yielding of the stirrups and buckling of the longitudinal bars. The local buckling of the steel occurred due to the lack of concrete protection, and then a large amount of concrete in the compression zone was crushed. At the end of test, the lateral load dropped rapidly and specimens lost bearing capacity. However, the core concrete has little destruction due to the restraint of structural steel located in the center zone of cross section.

Shear-bond failure occurred in specimens T-6 and T-8. At the first cycle of μ=1, when the lateral load increased to about 40% of maximum load, horizontal cracks appeared in the tensile side of the column end and extended to the front. Differing from bending failure, most of the horizontal cracks developed into inclined cracks with the increasing of cyclic load. Moreover, when the inclined cracks extended to the steel flange, the cracks became steep suddenly and developed to vertical cracks along the upwards direction of the flange with an increasing width, and the vertical crack spread much quicker than the inclined crack, which is attributed primarily to the bond-slip between structural steel and concrete. With the increasing of lateral load, vertical cracks extended to the upper column and penetrated along the height of the column, which led to splitting cracks. Meanwhile, the spalling of mass concrete was caused by the separation of steel and external concrete. At cycles of μ=4, the bearing capacity of the specimen dropped rapidly and pronounced failure. Owing to the rapid spalling of the concrete, the bearing capacity of structural steel and reinforcement is not fully utilized and the bearing capacity of the specimen has lost, this demonstrates a poorer ductility than bearing and shear-compression failure.

Shear-compression failure occurred in specimens T-4 and T-9. The failure process was as follows. At first cycle of μ=1, horizontal cracks were observed in the column lower end firstly. With the increasing of lateral load, the initial cracks extended to the front and inclined approximately along the direction of 45 degrees, which formed a large number of inclined cracks. Due to the action of cyclic load, these slightly inclined cracks formed cross inclined cracks on the front of the columns, and cut the abdomen concrete into some small compression prisms. As the lateral load increases, inclined crack spread rapidly with an increasing width. Then certain apparent "X" shaped cross inclined cracks were observed. At cycles of μ=4, when the lateral load reached the ultimate bearing capacity, small prisms was crushed, which led to the destruction suddenly. However, structural steel, stirrups and longitudinal bars did not yield in the entire process. The specimen destroyed rapidly and possesses a poor ductility.

Shear-composition failure, the combination of shear bond and shear-compression failure, occurred in T-7, T-10 and T-11. Similar to shear-compression failure, horizontal cracks developed into inclined cracks on the front of the columns. Due to unsymmetrical steel shape, one flange was wider than the others, which resulted in an increasing width of cracks when a part of inclined cracks extended to the wider steel flange side. Then inclined cracks became steep and spread upward to the vertical cracks. In the end, it formed splitting cracks which makes the shear-bond failure occurred on the side of wider flange. As inclined cracks in the narrower side extended to the flange, the inclined cracks intersected with the cracks which were extended from the wider flange side and developed into a main cross inclined crack owing to the weak bearing capacity of narrower flange. At last, the prism between critical inclined cracks was crushed and the shear-compression failure occurred on the narrower flange side. The coexistence of two kinds of shear failure is the obvious characteristic of concrete-encased composite column with the unsymmetrical steel section. The two failures associate with each other, and the correlation degree is affected by various parameters.

3.2. Strain distribution

During the test, the strain distributions with the same failure mode were similar. Thus, for ease of presentation, only one specimen is shown for each failure mode.

3.2.1. concrete

As shown in Fig. 5, concrete strain distribution of different positions along cross-section at column bottom was measured by attached strain gauges on concrete surface. The strains were measured at the distance of 90mm, 150mm, 210mm, 270mm, respectively, from the column side face. Fig. 8 shows the strain distribution at different loading stages tested on typical specimens with three kinds of failure mode respectively.

The failure mode of specimen T-3 was bending failure. Before the load reaches 80% of the maximum load, the concrete strain at various depth of the cross section presents a linear distribution. Moreover, the strain distribution accords with plane cross section assumption and the position of the neutral axis remain unchanged. At the first cycle of $\mu = 4$, when the lateral load reached about 80% of the maximum load, the slip between steel and concrete leaded to the movement of neutral axis and strain distribution deviating from a straight line. However, the strain distribution of a part of sections below the compressed flange kept straight.

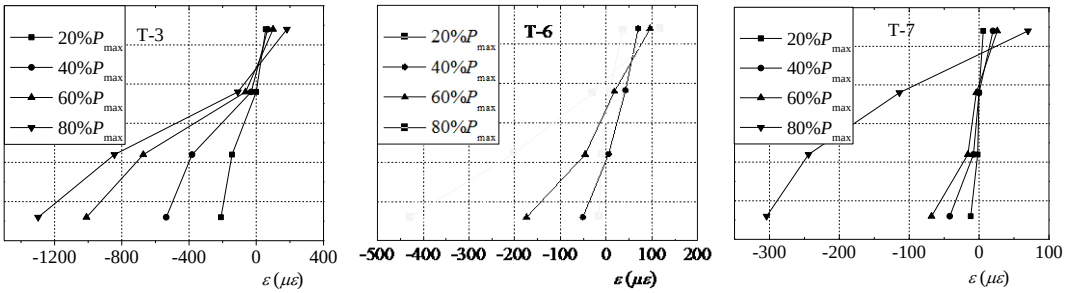

Fig. 8 Strain distributions of concrete along cross-section.

The failure mode of specimen T-6 was shear bond failure. The position of the neutral axis maintain invariable in the early stage of loading. However, the section strain along the depth can not satisfy the linear distribution because of the bond slip between steel and concrete. At the first cycle of $\mu = 3$, when the load reaches to 60% of the maximum load, the strain of concrete far away the neutral axis increases rapidly and deviates the line distribution further.

The failure mode of specimen T-9 is shear-compression. The section strain does not satisfy the assumption of plane cross section. With the appearance and development of inclined cracks, the strain distribution of concrete section at different depth presents an irregular curve distribution.

The results indicates that when bending failure occurred, the reached concrete strain is obvious greater than that in shear-bond failure and shear-compression failure. The concrete strain increases significantly in the latter two failures at the late stage of loading. It reflects that concrete possess a better deformation capacity and displacement ductility in bending failure.

3.2.2. Structural steel and reinforcement

Fig. 9 shows the measured principal values of the strain rosettes C1 attached to the steel web and that of the strain gauge A2 attached to hoop of specimen T-5, T-6 and T-9. The distribution of the strains in steel web and loops are shown. The test results showed that the strains were non-uniformly developed. It can be observed that when loaded at the positive direction the value of steel web strain was smaller than that at the negative direction. This phenomenon illustrates that the unsymmetrical steel section affect the strain distribution.

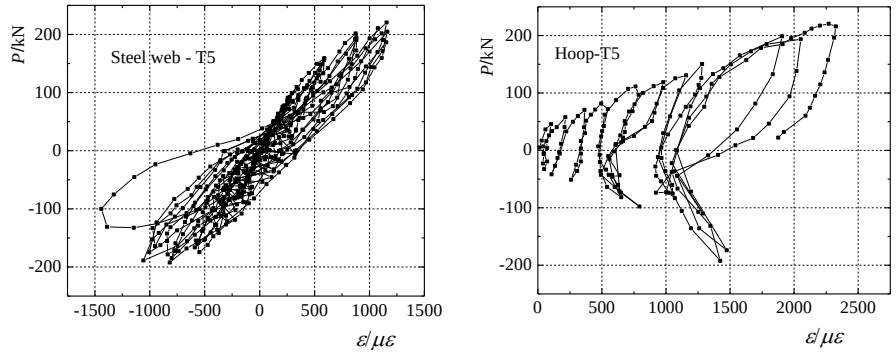

(a) Specimen T-5

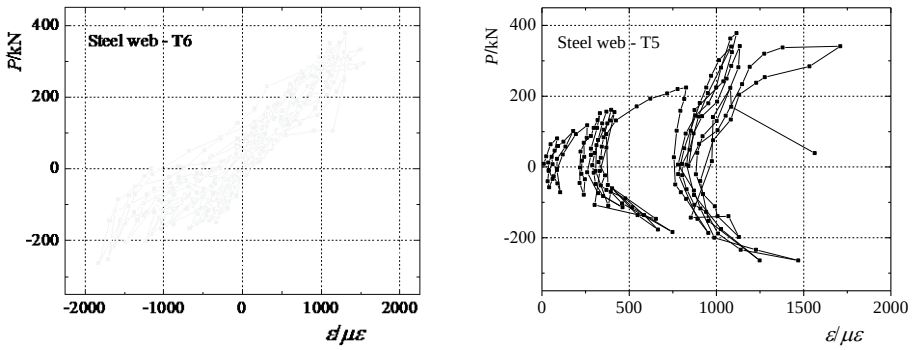

(b) Specimen T-6

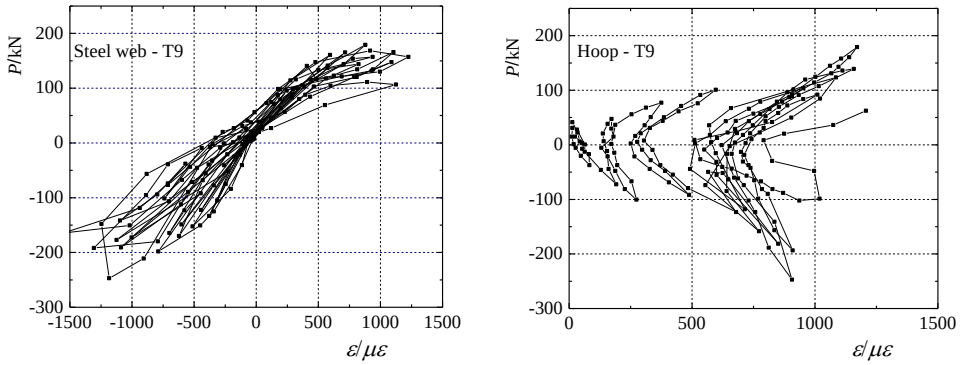

(c) Specimen T-9

Fig. 9 Strain distribution of steel web and hoop

It was found that the specimens showed an essentially linear behavior at early stage of loading, particularly before the load arriving at about 35% of maximum load. Local yielding started to develop in the steel web and hoops when the load arriving at about 60% of maximum load. The value of strain increased until the failure occurred, which indicated that cross ties are needed to restrict the inner concrete.

There is also something different on strain distribution among specimens with different failure mode. At the failure stage of loading, the strain value of steel web was largest when experienced a shear-compression failure, the strain value of hoop was largest when experienced a bearing failure.

3.3. Hysteretic curve

Hysteretic curve is a load-displacement relationship curve of the specimen under cyclic loading. As shown in Fig. 10, the hysteretic curve is described by the measured lateral load and displacement at the top end of the column, which is the important presentation of seismic performance. Among all the specimens, the test of specimen T-12 failed for loading equipments trouble, specimen T-10's data at positive loading direction did not acquired because of careless data input.

All the specimens have some hysteretic characteristics in common: at the early stage of loading, the specimens are in elastic stage and a linear relationship between load and displacement is presented. The residual deformation is small after unloading. The loading curve coincides with the unloading curve, and positive and negative hysteresis loop keeps essential symmetrical. With the increasing of load, the curve deviates from a straight line. After the cracking of concrete, the specimens enter into the elastic-plastic stage. The residual deformation exists in unloading process and the area of hysteresis loop increases gradually. The stiffness does not obviously deteriorate before yielding. However, the load decreases on the latter two cycles compared with the first cycle under each displacement loading level, which indicates strength deteriorate. Due to the increasing of loading displacement and the spalling of outer concrete, the hysteretic curve gradually inclines to the horizontal axis, which presents significant stiffness degeneration while the unsymmetrical phenomenon of hysteresis loop on two directions is particularly noticeable. After the load reaches the ultimate load, the hysteresis curve becomes plumper which demonstrates a good energy dissipation capacity.

Compared with axial compression load level, transverse reinforcement and cross tie, shear span ratio is the most important factor to determine the shape of hysteresis curve. In Fig.10, the hysteresis curve of T-4 with higher shear span ratio is plumper than T-9 with lower shear span ratio. For the specimens with lower shear span ratio, the arched shape of hysteresis curve is presented with a "narrow" hysteresis loop area and the curves on positive and negative direction are apparently unsymmetrical.

Specimens with lower axial compression level have plumper hysteresis curve, larger ultimate displacement and better elastic-plastic deformation capacity. Among the specimens with T-shaped steel section, hysteresis curve of T-3 is obvious plumper than T-4. The ultimate displacement of T-3 reaches 50mm while the latter is less than 40mm.

When the other parameters are the same, higher transverse reinforcement ratio can improve hysteretic behavior. The loading cycle times as well as the ultimate displacement of specimen T-8 are greater than T-9.

The presence of cross tie has little effect on shape of hysteretic curve for columns with T-shaped steel. The cross tie enhances ultimate bearing capacity by confining the concrete and preventing buckling of the longitudinal bar.

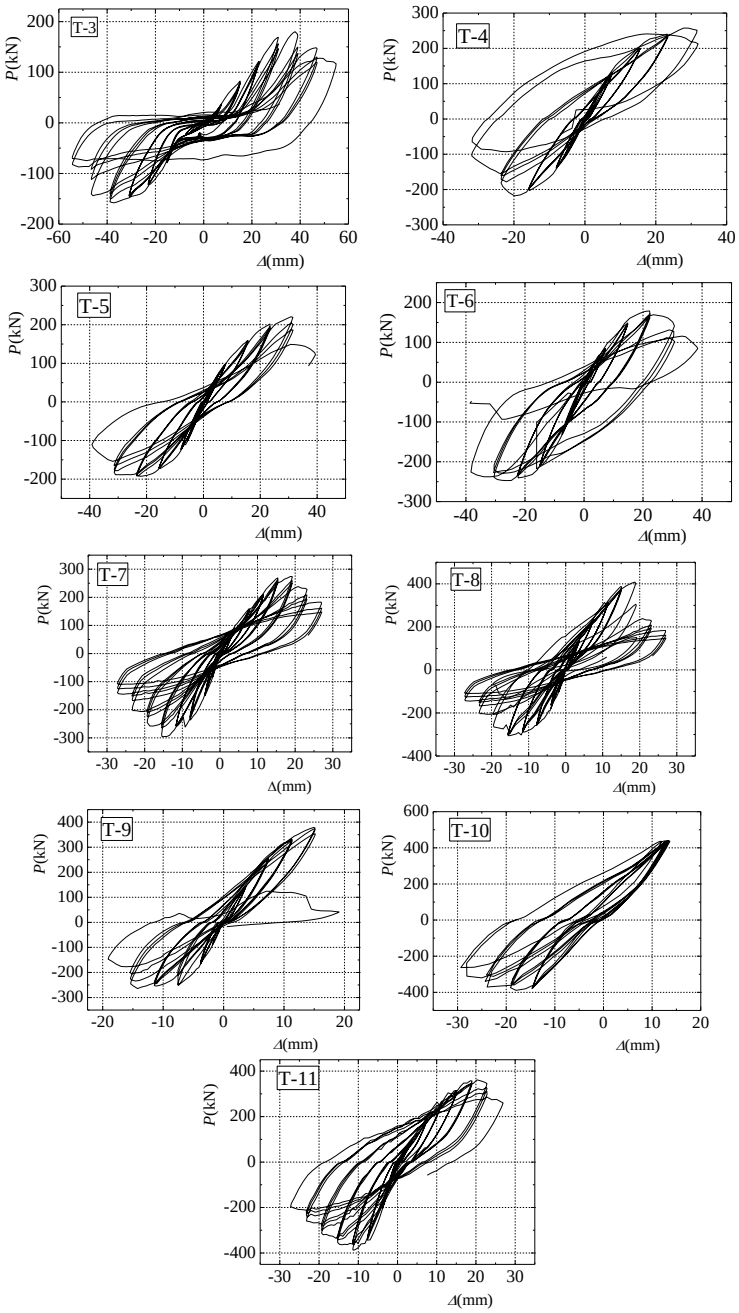

Fig. 10 Load-displacement hysteresis loops of specimens.

3.4. Skeleton curve

The skeleton curve reflects the characteristic of stress and deformation at different stages of specimens, which is the important basis to determine the feature point in restoring force model. In analysis of skeleton curve, positive loading direction is defined when the wider flange of inner structural steel subjected to tension, while negative loading direction is defined when subjected to compression. Fig. 11 shows skeleton curves for all specimens except T-12.

As shown in Fig. 11, specimens T-2 and T-8, without cross tie, have same axis load level and stirrup ratio. The shear span ratio is 2.5 and 2.0 for specimens T-2 and T-8, respectively. It can be seen that the ascent and descent stages of the curve are flatter for the specimen with higher shear span ratio. However, specimen with lower shear span ratio has higher ultimate load but greater load attenuation.

Fig. 11 (a) shows comparison of T-1 and T-2, whose axis load level are 2.0 and 0.4 respectively, which indicated that specimen with lower axis load level possess flatter curve, smaller ultimate load and larger ultimate displacement.

The stirrup ratio of specimens T-2 and T-4 are 1.675% and 1.256% respectively. It can be concluded that the specimens with higher stirrup ratio have a larger ultimate bearing capacity and limit deformation.

Skeleton curves of specimens T-3 and T-5 are shown in Fig. 11(a), which has the same axis load level and stirrup ratio. It is observed that the specimen with cross tie has larger ultimate bearing capacity and gentler inclined descent curve, which indicates slower strength degradation.

3.5. Ductility coefficient

Ductility is an important index of structural seismic behavior. To evaluate deformation capacity of specimens, a displacement ductility ratio is adopted. As shown in Fig. 12, the yield point is determined by equivalent internal energy method[28], and the failure point is based on the load which falls to 85% of the ultimate load. Displacement ductility is defined as ratio of failure displacement to yielding displacement of the column, $\mu=\Delta_u/\Delta_y$. The peak strengths P_u, yield displacements Δ_u, maximum displacements Δ_{max} and displacement ductilities μ are presented in Table 3. The values of P_u, Δ_u, and u in Table 3 were calculated from the envelope curves for the positive and negative loading.

Due to unsymmetrical arrangement of the structural steel in specimens, the ductility under two opposite loading directions differs and ductility coefficient is significantly larger when negative loaded. In this paper, the smaller side of ductility coefficient is adopted.

It can be seen from Table 3, with increasing of shear span ratio, ductility progressively improves. The influence of ductility coefficient caused by shear span ratio mainly reflects on the failure mode. Flexural failure only occurred in specimens with higher shear span ratio, but shear failure happened in all specimens with lower shear span ratio. Under combined action of moment and shear, the bending moment dominates the failure mode in specimens with higher shear span ratio, which leads flexural failure with better ductility. For specimens with lower shear span ratio, shear dominates failure mode. On one hand, shear results in an appearance of inclined cracks at the end of specimens and the cracks developed into staggered main inclined crack. Meanwhile, the prism concrete between inclined cracks is crushed, brittle inclined compression failure occurred.

On the other hand, the concrete of compression side is not crushed owning to the small bending moment, which makes the slightly inclined cracks in the side of external concrete develop upward along the steel flange sufficiently and rapidly. At last, the bond failure with poor ductility occurred.

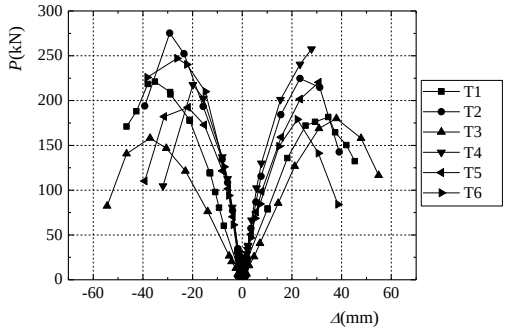

(a) T-shaped steel section specimens (λ=2.5)

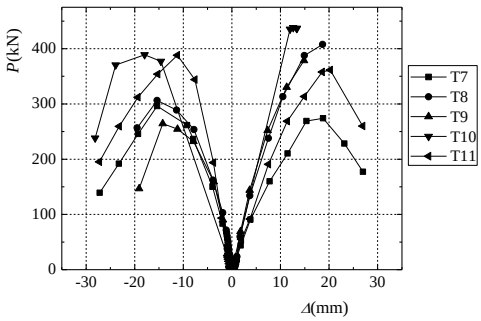

(b) T-shaped steel section specimens (λ=2.0)

Fig. 11 Comparison of skeleton curves in accordance with shear span ratio: (a) λ=2.5; (b) λ=2.0

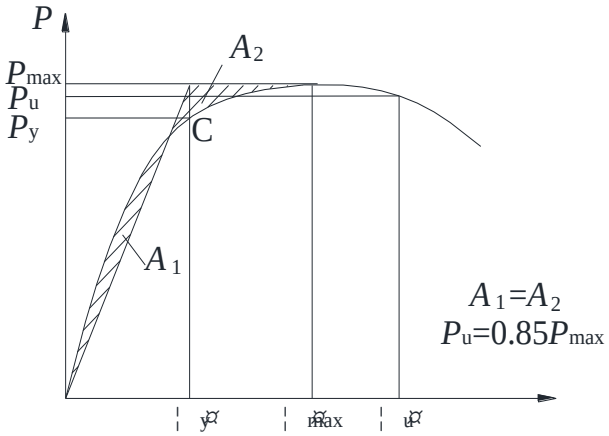

Fig. 12 Definitions of yield point and failure point

Table 3 Characteristic points of skeleton curves and ductility coefficient

Specimen	Load direction	P_y/kN	Δ_y/mm	P_{max}/kN	Δ_{max}/mm	P_u/kN	Δ_u/mm	$\mu=\Delta_u/\Delta_y$
T-1	Negative	77.44	9.96	181.55	34.66	154.32	41.06	4.12
	Positive	97.06	10.79	221.19	35.13	188.01	43.07	3.99
T-2	Negative	128.81	9.30	224.66	23.22	190.96	34.09	3.67
	Positive	150.86	10.29	275.27	29.19	233.98	35.63	3.46
T-3	Negative	80.50	13.61	180.12	37.89	153.10	48.70	3.58
	Positive	76.44	14.15	158.03	37.09	134.33	46.93	3.32
T-4	Negative	/	/	257.49	27.89	218.87	/	3.41
	Positive	138.50	8.44	217.69	19.84	185.03	24.17	2.86
T-5	Negative	100.59	8.29	220.49	30.84	187.41	34.33	4.14

T-6	Positive	126.34	8.72	192.46	21.84	163.59	33.33	3.82
	Negative	95.38	8.39	179.03	22.20	152.18	29.84	3.56
T-7	Positive	163.50	/	247.08	26.23	210.02	43.82	4.05
	Negative	127.93	5.86	273.98	18.76	232.89	22.86	3.90
T-8	Positive	163.75	4.70	296.05	15.38	251.65	19.67	4.18
	Negative	/	/	407.82	18.69	346.65	/	3.79
T-9	Positive	227.58	6.83	306.21	15.40	260.28	19.83	2.90
	Negative	157.37	4.23	378.45	14.85	321.68	15.43	3.65
T-10	Positive	200.75	6.29	264.32	14.23	224.68	15.99	2.54
	Negative	/	/	438.14	12.62	372.42	/	3.99
T-11	Positive	231.88	8.41	389.11	17.96	330.74	24.31	2.89
	Negative	217.05	8.85	361.46	20.24	307.24	24.06	2.72
	Positive	227.28	4.74	388.07	11.21	329.86	18.57	3.92

The ductility coefficient decreases with the increasing of axial compression. From Table 3, as axial compression level increases from 0.2 to 0.4, for example T-3 and T-4, T-1 and T-2, ductility coefficient drop about 12.5%. In general, the impact of high axial compression level on ductility coefficient is more outstanding.

On one hand, the predetermined friction produced by internal aggregate and mortar of concrete under axis load, so that it delays the tension cracking of the tiny bond crack. On the other hand, the large axial load restrains the development of inclined crack on the specimen surface. However, the delay and restrain can only enhance the crack resistance capacity of specimens, and makes the internal energy in the specimen unable to dissipate. When the lateral load increases to the ultimate load, the suddenly releasing of internal energy makes the specimen destroy abruptly without obvious omen, which leads to the worst ductility of the specimen.

It is indicated that the increasing of stirrup ratio and the presence of cross ties can enhance the ductility. It mainly reflects on the improvement of mechanical behavior of the concrete, the state of triaxial compression of the inner concrete caused by stirrup and cross tie, and the increasing of ultimate stress and ultimate strain, which improve the ductility of the specimen.

3.6. Stiffness degradation

Based on the experimental results the mean value of the stiffness for the ith cycle has been evaluated by the following ratio:

$$K = \frac{\left|P^{+}_{\max,i}\right| + \left|P^{-}_{\max,i}\right|}{\left|\Delta^{+}_{\max,i}\right| + \left|\Delta^{-}_{\max,i}\right|} \tag{4}$$

The stiffness of each cycle was then normalized with respect to the stiffness of the first cycle K_1, thus providing a measure of the stiffness degradation. The relationships between the K/K_1 ratio and the imposed displacement are plotted in Fig. 13.

Fig. 13(a) compares the stiffness and axial compression level. As presented in the Fig. 13(a), the specimens with higher axial compression load experienced stiffness degradation at early stage of loading. This is mostly attributable to the restriction on concrete crack by axial compression load applied on the specimens. However stiffness degradation is more evident in the specimens with higher axial compression load. The result indicated that to improve the axial compression load can improve the bearing capacity of the specimens within a certain range, but will aggravate stiffness degradation at the failure stage of loading.

Fig. 13(b) shows compare of stiffness degradation curves and shear span ratio. With the lateral load increases, Compared with specimen T-9 and T-10, specimen T-4 with larger shear span ratio was more gradual, which indicated the larger shear span ratio can delay stiffness degradation. Higher shear span ratio may decrease bearing capacity slightly, but the stiffness degradation process can be delayed. It is indicated that small shear span ratio should be avoided in the earthquake zone.

Fig. 13(c) shows compare of stiffness degradation curves and stirrup ratio. Stirrup ratio has little effect on the initial stiffness of the specimen, and the specimen stiffness degradation was not obvious before specimen yield. With the loading displacement increases, stiffness of specimen with smaller stirrup ratio degraded faster, but the affection is not obvious. It is indicated that higher stirrup ratio may be applied to delay stiffness degradation in the earthquake zone.

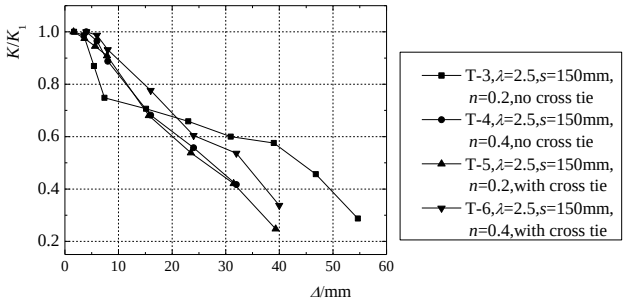

(a) Stiffness and axial load level

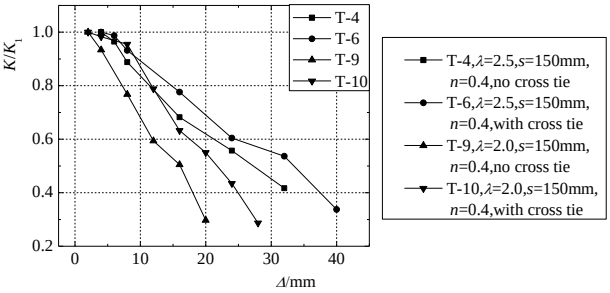

(b) Stiffness and shear span ratio

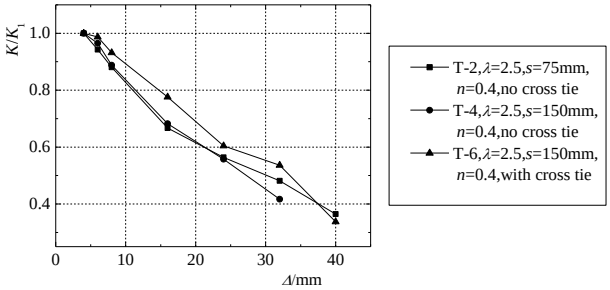

(c) Stiffness and stirrup ratio level

Fig. 13 Relationships between the stiffness and displacement

3.7. Energy dissipation capacity

The energy dissipation capacity, shown in Table 3, is defined as the dissipation capability of seismic energy in an earthquake, which is the important basis of assessment for the seismic behavior. The analysis of energy dissipation capacity adopts equivalent viscous damping coefficient h_e by the following equations[28].

$$h_e = \frac{1}{2\pi} \cdot \frac{S_{(ABC+CDA)}}{S_{(OBE+ODF)}} \tag{4}$$

where $S_{(ABC+CDA)}$ represents the area of a hysteretic loop as the shadow area shown in Fig. 14. $S_{(OBE+ODF)}$ is the area of a triangle which is corresponded to the maximum lateral load and the maximum horizontal displacement point of hysteresis loop on upper and lower sides. The surrounded area of dashed line and horizontal axis is shown in Fig. 14.

Fig. 15 is the curve of the relationship between the equivalent viscous damping coefficient and displacement for the specimens with different displacement levels under the first cyclic loading. It is shown that the average equivalent damping coefficient value is 0.265 when the specimens fail, and some of specimens reach above 0.4. It illustrates that concrete-encased composite columns with T-shaped steel section have good energy dissipation capacity. With the increasing of displacement, the equivalent damping coefficient of all specimens presents an upward trend, and the trend is obvious in the specimen with higher shear span ratio rather than lower shear span ratio. However, as the axis compression load increases, the equivalent damping coefficient of all specimens decreases. The improvement of stirrup ratio has a great effect on the increasing of equivalent damping coefficient, but the equivalent damping coefficient is not related to the presence of the cross tie.

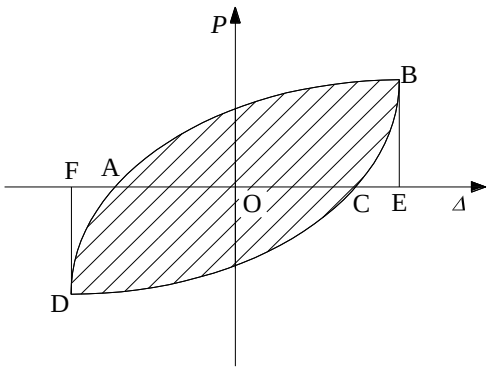

Fig. 14 Equivalent viscous damping coefficient h_e.

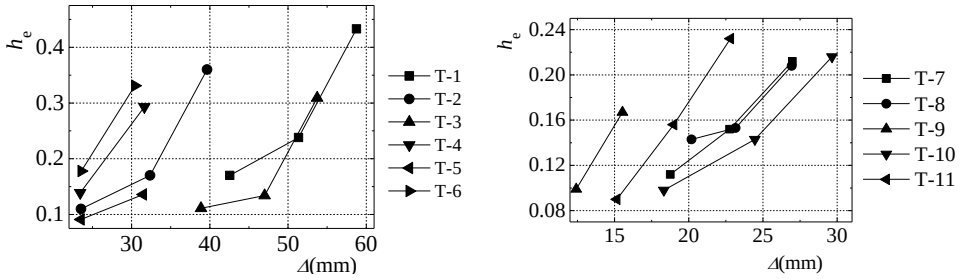

Fig. 15 Equivalent damp ratio of specimens

4. Summary and Conclusions

The following conclusions are concluded by cyclic load tests on twelve concrete-encased composite columns with T-shaped steel section.

Concrete-encased composite columns with T- shaped steel section possess good ductility, but the unsymmetrical phenomenon of hysteresis loop is evident. The average equivalent damping coefficient is above 0.26, energy dissipation capacity is better than normal reinforced concrete columns. The failure mode of columns with T-shaped steel section contains bonding failure, shear-bond failure, shear-compression failure and shear-composition failure. Shear span ratio and structural steel shape determine failure modes.

The hysteresis curves are affected by the level of shear span ratio and the applied axial compressive load. With the increase of shear span ratio, hysteresis curve becomes plumper, ultimate deformation capacity and energy dissipation capacity become better. With the increase of axis load, ultimate strength improves, but strength and ductility decrease rapidly on descending stage. Meanwhile, the influence of axis load level on specimens with T-shaped steel section is greater than specimens with L-shaped steel section. The presence of cross tie has a great improvement on seismic behavior for concrete-encased composite columns with unsymmetrical steel section.

The ultimate strength, ductility and energy dissipation capacity can be enhanced by providing the cross ties and decreased spacing of the hoops. This is attributed primarily to the increased confinement provided by the transverse reinforcement. However, the enhancement is not evident for specimens with L-shaped steel with low shear span ratio. Therefore, some strict construction measures should be taken in concrete-encased composite short columns with L-shaped steel section in seismic region.

Acknowledgements: This research was funded by National Natural Science Foundation of China (Grant No. 51108041, 51478048), Young and Middle-aged Scientific and Technological Innovation Team Foundation of Hubei Province of China (Grant No. T201303) and their support is gratefully acknowledged.

References

[1] Deierlein GG, Noguchi H. Overview of US-Japan research on the seismic design of composite reinforced concrete and steel moment frame structures, Journal of Structural Engineering, 2004, No. 2, Vol. 130, pp. 361-367.

[2] Shanmugam NE, Lakshmi B. State of the art report on steel–concrete composite columns, Journal of Constructional Steel Research, 2001, No. 10, Vol. 57, pp. 1041-1080.

[3] Nie J, Tao M, Huang Y, et al. Research advances of steel-concrete composite structural systems, Journal of Building Structures, 2010, No. 6, Vol. 31, pp. 71-80 (in Chinese).

[4] Lu W, Han J, Lu X, et al. Shaking table model test on Palms together dagoba at Famen Temple, Jianzhu Jiegou Xuebao (Journal of Building Structures), 2011, No. 3, Vol. 32, pp. 90-98 (in Chinese).

[5] Chen CC, Lin NJ. Analytical model for predicting axial capacity and behavior of concrete encased steel composite stub columns, Journal of Constructional Steel Research, 2006, No. 5, Vol. 62, pp. 424-433.

[6] Elghazouli AY, Treadway J. Inelastic behaviour of composite members under combined bending and axial loading, Journal of Constructional Steel Research, 2008, No. 9, Vol. 64, pp. 1008-1019.

[7] Ellobody E, Young B, Lam D. Eccentrically loaded concrete encased steel composite columns, Thin-Walled Structures, 2011, No. 1, Vol. 49, pp. 53-65.

[8] Charalampakis AE, Koumousis VK. Ultimate strength analysis of composite sections under biaxial bending and axial load, Advances in Engineering Software, 2008, No. 11, Vol. 39, pp. 923-936.

[9] Kim CS, Park HG, Chung KS, et al. Eccentric axial load testing for concrete-encased steel columns using 800 MPa steel and 100 mpa concrete, Journal of Structural Engineering, 2011, No. 8, Vol. 138, pp. 1019-1031.

[10] Dundar C, Tokgoz S, Tanrikulu AK, et al. Behaviour of reinforced and concrete-encased composite columns subjected to biaxial bending and axial load, Building and environment, 2008, No. 6, Vol. 43, pp. 1109-1120.

[11] Hsu HL, Jan FJ, Juang JL. Performance of composite members subjected to axial load and bi-axial bending, Journal of Constructional Steel Research, 2009, No. 4, Vol. 65, pp. 869-878.

[12] Jianyang X, Junhua L, Hongtie Z. Experimental study on the performance of steel reinforced high-strength concrete columns under low cyclic reversed loading, China Civil Engineering Journal, 2007, No. 7, Vol. 40, pp. 11-18 (in Chinese).

[13] Shim CS, Chung YS, Yoon JY. Cyclic behavior of prefabricated circular composite columns with low steel ratio, Engineering Structures, 2011, No. 9, Vol. 33, pp. 2525-2534.

[14] Chen C, Wang C, Sun H. Experimental study on seismic behavior of full encased steel-concrete composite columns, Journal of Structural Engineering, 2014, No. 6, Vol. 140, 04014024.

[15] Zixiong G, Huang L, Yang L. Experimental study on seismic behavior of SRC columns with different stirrup configuration, Journal of Building Structures, 2010, No. 4, Vol. 31, pp. 110-115 (in Chinese).

[16] Mao X, Kodur V K R. Fire resistance of concrete encased steel columns under 3-and 4-side standard heating, Journal of Constructional Steel Research, 2011, No. 3, Vol. 67, pp. 270-280.

[17] Young B, Ellobody E. Performance of axially restrained concrete encased steel composite columns at elevated temperatures, Engineering Structures, 2011, No. 1, Vol. 33, pp. 245-254.

[18] Karimi K, Tait M J, El-Dakhakhni WW. Analytical modeling and axial load design of a novel FRP-encased steel–concrete composite column for various slenderness ratios, Engineering Structures, 2013, Vol. 46, pp. 526-534.

[19] Marinopoulou AA, Balopoulos VD, Kalfas CN. Simulation of partially encased composite steel–concrete columns with steel columns, Journal of Constructional Steel Research, 2007, No. 8, Vol. 63, pp. 1058-1065.

[20] ACI Committee 318. Building code requirements for structural concrete (ACI 318-05) and commentary (ACI 318R-05)[C]. American Concrete Institute, 2005.

[21] American Institute of Steel Construction. Load and resistance factor design specification for structural steel buildings (3rd ed) [C]. AISC, Chicago, 1999.

[22] YB 9082-2006 (2006). Technical specification of steel-reinforced concrete structures, National Development And Reform Commision of the PRC, Beijing, China.

[23] JGJ 138-2001. Technical Specification for Steel Reinforced Concrete Composite Structures, Beijing, Architecture Industrial Press of China; 2001.

[24] Architectural institute of Japan. Standard for the calculation of steel-reinforced concrete structures (AIJ-SRC) [C]. AIJ, Tokyo, 2010.

[25] Roik K, Bergmann R. Design method for composite columns with unsymmetrical cross-sections, Journal of Constructional Steel Research, 1990, No. 1, Vol. 15, pp. 153-168.

[26] ENV 1994-1-1. Common unified rules for composite steel and concrete structures (EUROCODE 4) [C]. European Committee for Standardization, Brussel, 1994.

[27] GB/T228.1-2010. Metallic materials-tensile testing-Part 1: method of test at room temperature. Beijing, China Standard Press, 2011 [in Chinese].

[28] JGJ101-96. Specification for seismic test method. Beijing, Architecture Industrial Press of China, 1997. (in Chinese).